Received: 26 May 2024 | Revised: 22 August 2024 | Accepted: 19 September 2024

DOI: 10.1111/jace.20190

Journal of the American Ceramic Society

RESEARCH ARTICLE

Densification, deformation, and delamination during co-sintering process of metal–ceramic laminates

Chao Liu[1] | **Yuanbin Deng**[1] | **Daniel Gruner**[2] | **Anke Kaletsch**[1] | **Tim Gestrich**[2] | **Christoph Broeckmann**[1]

[1]Institute for Materials Applications in Mechanical Engineering (IWM), RWTH Aachen, Aachen, Germany

[2]Fraunhofer Institute for Ceramic Technologies and Systems IKTS, Dresden, Germany

Correspondence
Chao Liu and Yuanbin Deng, Institute for Materials Applications in Mechanical Engineering (IWM), RWTH Aachen, 52062 Aachen, Germany.
Email: chao.liu1@rwth-aachen.de; y.deng@iwm.rwth-aachen.de

Funding information
German Research Foundation (DFG), Grant/Award Number: 441616349

Abstract

Today, there is a high demand and increasing trend for multifunctional composite materials and components due to the combination of a wide range of favorable properties. However, undesired deformation leading to delamination, curvature, cracks, or even complete fracture frequently occurs during the co-sintering process of metal–ceramic laminates (MCLs). To solve these issues, experimental work highly relies on the time-consuming trial-and-error principle. This work aims to develop a thermo-mechanical-metallurgical model capable of predicting the densification, deformation, and delamination of MCLs during the co-sintering process. It is found that the developed model successfully considers the inhomogeneous relative density distribution and phase transformation of the steel tape. In addition, a thin interlayer formed by a mixed slurry in the MCLs is modeled as cohesive elements to simulate the delamination process. The developed model is systematically validated by the experimental measurements and observations in terms of densification, deformation, and delamination during the co-sintering process of the investigated laminate variants.

KEYWORDS

cohesive element, deformation, delamination, densification, finite element modeling, metal–ceramic laminates, transformation plasticity

1 | INTRODUCTION

Nowadays, there has been an increasing trend and high demand for multifunctional composite materials and components, which are produced by laminating and co-sintering of different components.[1] This is due to the fact that the combination of a wide range of favorable properties gives metal–ceramic composites a higher degree of flexibility than single individual materials. For instance, the combination of metals and ceramics enables the production of composites with insulation properties and local electrical conductivity at the same time. In addition, the brittle fracture behavior of ceramics can be positively influenced by the combination of metals to achieve high toughness/damage tolerance.[2] In principle, metal–ceramic laminates (MCLs) exhibit increased stress resistance and reliability in comparison to purely brittle ceramic material, as the metallic component is able to deform plastically and thus deflect or even stop the cracks that occur and propagate in the ceramic component.[2] Currently, such laminates

This is an open access article under the terms of the Creative Commons Attribution License, which permits use, distribution and reproduction in any medium, provided the original work is properly cited.
© 2024 The Author(s). *Journal of the American Ceramic Society* published by Wiley Periodicals LLC on behalf of American Ceramic Society.

have essentially been produced following the procedure of tape casting, lamination, debinding, and co-sintering. By using green tapes with different compositions, composite laminates with different materials and property gradients can be produced during the final debinding and co-sintering process.[3–5]

However, undesired deformation leading to delamination, curvature, cracks, or even complete fracture frequently occurs during the manufacturing process.[6–8] This deformation primarily results from different total shrinkages and shrinkage rates of combined materials. A wide range of factors influence the shrinkage and shrinkage rate of a material during a sintering process: the initial relative density distribution, the temperature gradient inside a component, the viscosity of a material, grain size distribution, as well as sintering stress. Moreover, large shear stresses at the interface between different materials may be induced due to incompatible Young's moduli, Poisson ratios, and coefficients of thermal expansion (CTE) of different materials. In addition, the phase transformation of steel components may further increase the shear stresses at the interface during co-sintering process. Once the shear stress exceeds the strength of the interface, damage initiates and propagates until the fracture energy of interface is completely dissipated, which indicates the occurrence of a complete fracture.

To avoid fracture and achieve a defect-free, near-net-shape layer composite design, previous studies have primarily relied on the trial-and-error principle from the perspective of experiments. For instance, Dourandish et al.[9] have investigated the possibility of pressureless sintering of compacted 3Y-TZP (with two particle sizes) with three different stainless steels (martensitic 17-4PH, austenitic 316L and 420 SS) under various sintering atmospheres (H_2, Ar, Ar+H_2, and vacuum). They found that the mismatch strain between 3Y-TZP and stainless steels during co-sintering can lead to bond cracking and joint failure. The joining of 3Y-TZP (with a particle size of 150 nm) to 420 SS under vacuum appeared to be most successful among all the investigated combinations. Another trial-and-error study was carried out by Slawik et al.[10,11] who used four different compositions of metallic slurries for tape casting and subsequent co-sintering with 3Y-TZP to obtain symmetric and asymmetric MCLs. The spherical metallic powder was milled in advance to modify the particle shape and increase its specific surface area so that a larger sintering strain can be obtained.[10] It was found that the relative density of zirconia layer in MCLs was reduced due to less shrinkage of the metallic layer. Moreover, cracks occurred in the ceramic layer due to mismatches in the strain rate. Nevertheless, manufacturing of defect-free MCLs with dense ceramic layers was still achievable by adapting the sintering behavior of metallic powder. The trial-and-error method usually results in a high failure-to-success ratio and needs a long development period. Therefore, there is a high demand for numerical methods that allow evaluation of the manufacturability and prediction of the deformation during the co-sintering process. On the component scale, the Finite Element Method (FEM) has been most commonly used to capture the densification and volumetric deformation of components during sintering. It allows reliable simulations of arbitrarily complex-shaped macroscale components. This is particularly valuable for complex composite parts or multilayer laminates, as they typically do not shrink isotropically.[12] This method has been successfully used to predict the shrinkage and geometry changes of bilayer components[13–16] or more complex structures.[17] In addition to sintering (densification) simulation, FEM is well-known to be capable of simulating the phase transformation and transformation-induced plasticity during heat treatment,[18] and delamination of composites by cohesive elements.[19,20] However, to the best knowledge of the authors, a combined thermo-mechanical-metallurgical model that simultaneously considers co-sintering with green density gradient, phase transformation, and interface properties has not yet been published.

The hypothesis of this work is that by correctly considering the initial relative density gradient of the metal layer and resulting anisotropic properties, the interlayer (modeled as cohesive elements) as well as the plastic strains (resulting from yielding, creep and phase transformation) of the metal layer during the cooling down, the densification, deformation, delamination of metal–ceramic laminates during the co-sintering can be numerically predicted with high accuracy. Therefore, the primary objective of this work is to develop a thermo-mechanical-metallurgical model capable of predicting the densification, deformation, delamination, and stress evolution of metal–ceramic laminates. In addition, we aim to obtain a better understanding of the causes of delamination during the co-sintering process based on the developed FE model.

2 | MATERIALS AND METHODS

2.1 | Production of laminates, optical dilatometry, and micrographs

The two materials under investigation are martensitic precipitation-hardened stainless steel 17-4PH and partially stabilized zirconia powder with uniform dispersion of 3 mol% yttria (commercial name TZ-3YS-E, 3 mol% yttria-stabilized tetragonal zirconia 3Y-TZP after sintering), produced by Sandvik Osprey, Ltd., and Tosoh, respectively. These two materials were selected to manufacture MCLs

RIGHTSLINK

15512916, 0, Downloaded from https://ceramics.onlinelibrary.wiley.com/doi/10.1111/jace.20190 by Rwth Aachen, Wiley Online Library on [28/10/2024]. See the Terms and Conditions (https://onlinelibrary.wiley.com/terms-and-conditions) on Wiley Online Library for rules of use; OA articles are governed by the applicable Creative Commons License

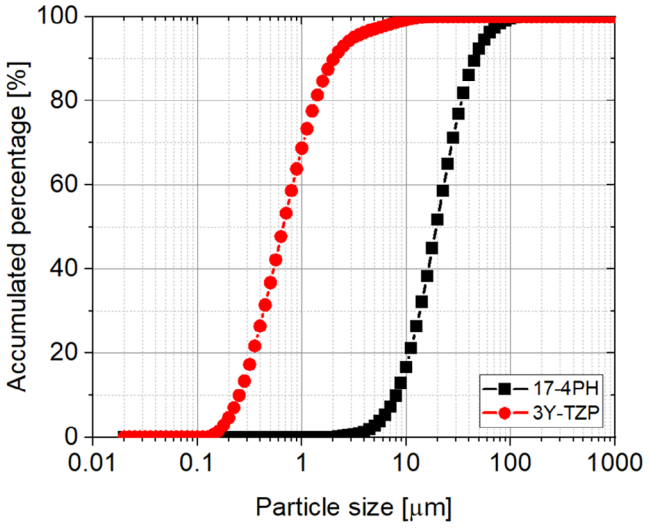


FIGURE 1 Particle size distribution of 17-4PH and 3Y-TZP powder used in this work.

because they have similar CTE and shrinkage rates.[21] Laser diffraction analysis using the Mastersizer 2000 (Malvern Panalytical GmbH) was carried out to determine the particle size distributions of the used powders. As shown in Figure 1, the particle size d_{50} and d_{90} of 17-4PH are 19.4 and 45.5 µm, respectively. In comparison, d_{50} and d_{90} of 3Y-TZP are 0.66 and 2.03 µm.

The production of 17-4PH and 3Y-TZP tapes was performed by tape casting. The suspensions for the casting were obtained by homogenizing the powder with a solvent (deionized water), dispersing agent (Dolapix CE 64; Zschimmer & Schwarz), polyvinyl alcohol binder (PVA; Mowiol 20–98; Ter Hell GmbH), plasticizing agent (glycerin; Carl Roth GmbH), defoaming agent (Foamaster F-111; BASF), and an additional wetting agent (Glydol; Zschimmer & Schwarz) for the ceramic suspensions. The optimized solids contents of the slurry suspensions were 22 vol% for 3Y-TZP and 23 vol% for 17-4PH. The tapes were cast by applying slurry onto a tape carrier using the doctor blade method where the blade gap was adjusted to 1.0 mm. Subsequently, the tapes were dried at ambient temperatures with 50% humidity. The corresponding drying time depends on the tape thickness. The single dried metal and ceramic tape had thickness of 0.32 and 0.41 mm, respectively. Afterwards, the dried green tapes of 17-4PH and 3Y-TZP were used to assemble three-layer composite laminates. The laminates were pre-laminated using a hand roller and then cold-rolled on a rolling mill to remove any air bubbles. The roll gap was set at 50 µm below the laminate thickness. Then the laminates were dried for at least 24 h at ambient temperature and 50% humidity between metal plates with a load of 10 kg. The geometrical configurations of the produced three-layer metal–ceramic laminates are schematically illustrated in Figure 2.

For the asymmetrical MCLs, while the interface between the same material was wetted with deionized water, a mixed interlayer of 50% metal and 50% ceramic slurry with a thickness of approximately 0.09 mm was applied as a laminating suspension between the metal and the ceramic tape, as shown in Figure 2A,B. The blue and white areas in the schematic representation of a single 17-4PH tape represent the bottom and top side with higher and lower relative density, respectively. This kind of "blue-white" contour to represent the relative density gradient in a single 17-4PH tape is further used in all investigated variants of laminates. For the symmetrical MCLs, the identical mixed interlayer that had been used for the asymmetrical MCLs, was applied between the metal and ceramic layers as shown in Figure 2C,D. To this end, four variants of three-layer green laminates were produced. The m-m-c, c-c-m, c-m-c, and m-c-m have a total thickness of approximately 1.14, 1.23, 1.32, and 1.23 mm, respectively.

For the measurements of the deformation and shrinkages, square green laminates with a dimension of approximately $8 \times 8 \times h$ mm^3 (h is the total thickness of each laminate) were prepared as specimens by cutting them out of the central area of the laminated tapes using a sharp blade. The shrinkage behavior and the deformation of the laminates during the sintering process were characterized by optical dilatometry where a heating microscope (EM201; HESSE instruments) was used. The specimen to be examined was placed in a tube furnace and illuminated from the front side, with the silhouette of the specimens being recorded using a CCD-camera from the back side. The width and height change of specimens during the debinding and sintering were recorded and determined from the silhouettes. Due to the low thickness of laminates leading to large uncertainties of measurement, the width change was chosen to represent the shrinkage in the following context. All the shrinkages are calculated along the project width in this work, if not mentioned otherwise. During the measurement, the tube furnace was purged with a gas mixture of 95% argon and 5% hydrogen (Varigon H5; Linde GmbH). The debinding of the laminates was performed with 5 K/min to 250°C and 2 K/min to 500°C, followed by 5 K/min to 1370°C and 30 min dwell time for the sintering process. The experimental set-up consisted of a laminate centered on a smaller alumina support.

Besides, two single 17-4PH tapes were pre-sintered at 1000°C to investigate the relative density distribution resulting from sedimentation effect during tape casting. The pre-sintered tapes were subsequently embedded in epoxy resin and then grinded with a diamond suspension down to 1 µm, followed by polishing with an oxide

RIGHTSLINK

15512916, 0, Downloaded from https://ceramics.onlinelibrary.wiley.com/doi/10.1111/jace.20190 by Rwth Aachen, Wiley Online Library on [28/10/2024]. See the Terms and Conditions (https://onlinelibrary.wiley.com/terms-and-conditions) on Wiley Online Library for rules of use; OA articles are governed by the applicable Creative Commons License

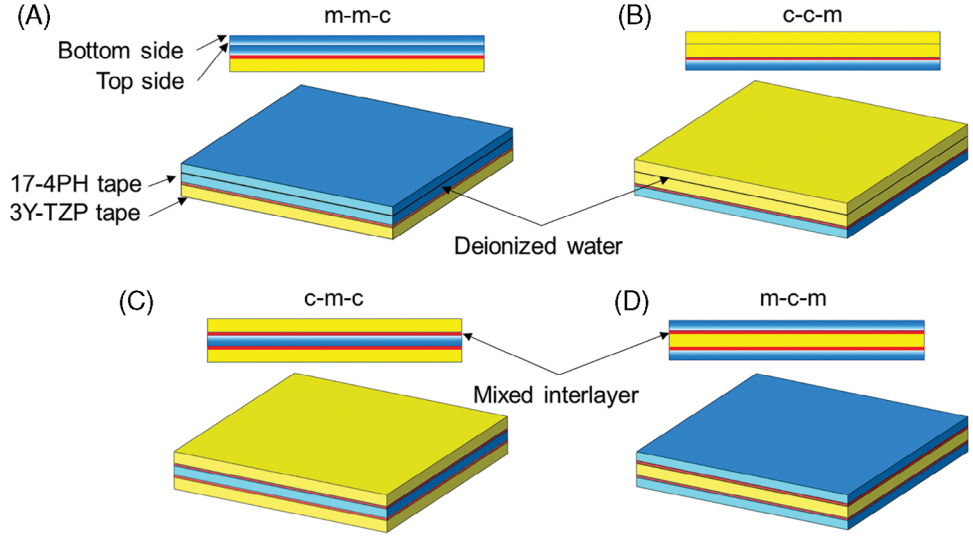


FIGURE 2 Layer arrangement of investigated laminates. (A and B) Asymmetric laminates with one mixed interlayer connecting tapes of different materials. Tapes of same materials are connected with deionized water. Blue and white represent the bottom and top side with higher and lower relative density of a single 17-4PH tape, respectively. (C and D) Symmetric laminates with two mixed interlayers connecting tapes of different materials.

polishing slurry. The images of the cross-section were taken using the Nikon EPIPHOT 300 (Nikon Metrology GmbH).

2.2 | Modeling of densification and implementation in FE simulation

As two different materials (ceramic 3Y-TZP, steel 17-4PH) are involved, different decompositions of strain increments for each material must be considered in the developed thermo-mechanical-metallurgical model. In terms of modeling, the mechanical interactions for 3Y-TZP, the increment of the total strain $\Delta\varepsilon_{ij}^{\text{total}}$ only consists of the increment of the elastic strain $\Delta\varepsilon_{ij}^{\text{el}}$, the viscoplastic strain $\Delta\varepsilon_{ij}^{\text{vp}}$, and the thermal strain $\Delta\varepsilon^{\text{th}}$:

$$\Delta\varepsilon_{ij}^{\text{total}} = \underbrace{\Delta\varepsilon_{ij}^{\text{el}} + \Delta\varepsilon_{ij}^{\text{vp}}}_{\text{Mechanical strains}} + \underbrace{\delta_{ij}\Delta\varepsilon^{\text{th}}}_{\text{Thermal strain}} \tag{1}$$

where δ_{ij} is the Kronecker delta. For the modeling of the mechanical interactions of 17-4PH, the increment of the total strain $\Delta\varepsilon_{ij}^{\text{total}}$ can be described as

$$\Delta\varepsilon_{ij}^{\text{total}} = \underbrace{\Delta\varepsilon_{ij}^{\text{el}} + \Delta\varepsilon_{ij}^{\text{vp}} + \Delta\varepsilon_{ij}^{\text{pl}}}_{\text{Mechanical strains}} + \underbrace{\delta_{ij}\Delta\varepsilon^{\text{th}}}_{\text{Thermal strain}} + \underbrace{\delta_{ij}\Delta\varepsilon^{\text{tr}} + \Delta\varepsilon_{ij}^{\text{tp}}}_{\text{Metallurgical strains}} \tag{2}$$

where $\Delta\varepsilon_{ij}^{\text{pl}}$ is the increment of the plastic strain due to yielding, $\Delta\varepsilon^{\text{tr}}$ is the strain of volume changes due to phase transformation, and $\Delta\varepsilon_{ij}^{\text{tp}}$ is the strain of transformation-induced plasticity. The following sections concern modeling the increment of the individual strain decompositions in Equations (1) and (2).

For both materials, densification can be modeled in a linear viscoplastic continuum framework proposed by Riedel et al.[22]:

$$\Delta\varepsilon_{ij}^{\text{vp}} = \left[\frac{S_{ij}}{2G_p} + \left(\frac{\sigma_m - \sigma_s}{3K_p}\right)\delta_{ij}\right]\Delta t \tag{3}$$

where S_{ij} and σ_m are the deviatoric and hydrostatic stress, respectively, G_p the shear viscosity, and K_p the bulk viscosity, both of which depend simultaneously on the temperature, grain size, and relative density, and Δt the time increment. The viscoplastic strain $\Delta\varepsilon^{\text{vp}}$ simulates the distortion and volume change of a component. In the FE simulation, the increment of the viscoplastic strain $\Delta\varepsilon_{ij}^{\text{vp}}$ is calculated in the Abaqus Subroutine CREEP:

$$\Delta\varepsilon_{ij}^{\text{vp}} = \Delta\bar{\varepsilon}^{\text{cr}} \cdot \frac{3S_{ij}}{2\tilde{q}} + \frac{1}{3}\Delta\bar{\varepsilon}^{\text{sw}}\delta_{ij} \tag{4}$$

where $\Delta\bar{\varepsilon}^{\text{cr}}$ is the uniaxial equivalent "creep" strain, $\tilde{q}$ the von-Mises stress, and $\Delta\bar{\varepsilon}^{\text{sw}}$ the volumetric swelling strain. A comparison between Equations (3) and (4) yields:

$$\Delta\bar{\varepsilon}^{\text{cr}} = \frac{\tilde{q}}{3G_p}\Delta t; \quad \frac{\partial\Delta\bar{\varepsilon}^{\text{cr}}}{\partial\tilde{q}} = \frac{\Delta t}{3G_p} \tag{5}$$

RIGHTSLINK

15512916, 0, Downloaded from https://ceramics.onlinelibrary.wiley.com/doi/10.1111/jace.20190 by Rwth Aachen, Wiley Online Library on [28/10/2024]. See the Terms and Conditions (https://onlinelibrary.wiley.com/terms-and-conditions) on Wiley Online Library for rules of use; OA articles are governed by the applicable Creative Commons License

$$\Delta\bar{\varepsilon}^{sw} = \frac{-p-\sigma_s}{K_p}\Delta t; \quad \frac{\partial\Delta\bar{\varepsilon}^{sw}}{\partial p} = -\frac{\Delta t}{K_p} \tag{6}$$

The partial differentiation of the term $\Delta\bar{\varepsilon}^{cr}$ and $\Delta\bar{\varepsilon}^{sw}$ is required for the calculation of the strain component in the next increment in Abaqus. Parameter p is the hydrostatic pressure that is the negative value of the hydrostatic stress σ_m. As can be seen from the above equations, in order to calculate the increment of the creep strain, the shear and bulk viscosity G_p and K_p of a material has to be determined first. The Rahaman model[23] is used to describe the uniaxial viscosity, as it best fits the experimentally measured data point from our previous study.[24] It can be written as

$$E_p = 9A_0 \exp\left(\frac{Q_\eta}{RT}\right) D^{m_2} \cdot f(\rho) \tag{7}$$

where $f(\rho)$ is a function of the relative density ρ and can be expressed as[23]

$$f(\rho) = \frac{\rho \exp[-3\alpha(1-\rho)]}{3\exp[-\alpha(1-\rho)] + \exp[-2\alpha(1-\rho)]} \tag{8}$$

The material parameters A_0 and grain growth exponent m_2 were obtained by fitting the uniaxial viscosity data of 3Y-TZP taken from.[24] Q_η is the activation energy of deformation for 3Y-TZP obtained from.[24] Parameter α is inversely proportional to the dihedral angle of 3Y-TZP and was obtained to be 4.57 from.[24] Furthermore R is the gas constant, T the temperature, and D the grain size. To obtain the shear and bulk viscosity, the expression of the viscous Poisson ratio proposed by Bordia and Scherer[25] was applied:

$$\nu_p = \frac{1}{2}\sqrt{\frac{\rho}{3-2\rho}} \tag{9}$$

To this point, the shear and bulk viscosity can be calculated by

$$G_p = \frac{E_p}{2(1+\nu_p)}; \quad K_p = \frac{E_p}{3(1-2\nu_p)} \tag{10}$$

As indicated in Equation (7), the viscosity depends on the grain size. The grain growth or grain coarsening is an important phenomenon during the sintering process of polycrystalline materials. It usually leads to a larger viscosity and a lower sintering stress at the final sintering stage, thus retarding the densification rate. The following equation from[26] is applied to describe the grain growth of the two materials in this work:

$$D = D_0 + \frac{k(\rho-\rho_0)^n}{D_0} \tag{11}$$

where k and n are two parameters fitted according to the plot of relative density and grain size. The sintering stress σ_s or sintering potential is described as the driving force for densification. It depends on the surface energy, grain size, and relative density. The equation of the sintering stress proposed by Shinagawa[27] was used:

$$\sigma_s = \frac{4\gamma}{\zeta D}\rho^{N_1}\left[\frac{\rho}{\rho_0}\cdot\frac{(1-\rho_0)}{(1-\rho)}\right]^{1/3} \tag{12}$$

where ζ and N_1 are two material parameters depending on the shrinkage behavior of the two materials. γ is the surface energy and ρ_0 the initial relative density. As can be seen from Equation (12), the sintering stress depends proportionally on the surface energy and is inversely proportional on the grain size. In addition, the following equation from[28] was applied to update the relative density after each time increment.

$$\rho(t+\Delta t) = -\rho(t)\cdot\Delta\varepsilon_{kk}^{vp} + \rho(t) \tag{13}$$

where $\Delta\varepsilon_{kk}^{vp}$ is the trace of tensor $\Delta\varepsilon_{ij}^{vp}$, which equals $\Delta\varepsilon_{11}^{vp} + \Delta\varepsilon_{22}^{vp} + \Delta\varepsilon_{33}^{vp}$.

2.3 | Modeling of yielding, creep and phase transformation, and transformation plasticity for 17-4PH

In the simulation, 17-4PH was modeled as an elastoplastic material in which the dataset of plastic strains and corresponding yield stresses at different temperatures measured by dilatometer DIL805 were imported in Abaqus. The plastic strains and the corresponding stresses at different temperatures were automatically captured in Abaqus. In addition, isotropic hardening of 17-4PH was assumed during the sintering process. Similar to the thermal conductivity and Young's modulus, the yield stress is also dependent on the relative density.[29] Therefore, the Balshin equation[30] was applied to describe the yield behavior of porous 17-4PH where the exponent m equals 3.5, which was explicitly specified in subroutine USDFLD. As such, the increment of the plastic strain $\Delta\varepsilon^{pl}$ from Equation (2) due to yielding can be obtained. The increment of creep strain of 17-4PH during the cooling down process was modeled by replacing Equation (5) by

$$\Delta\bar{\varepsilon}^{cr} = A\tilde{q}^N\Delta t; \quad \frac{\partial\Delta\bar{\varepsilon}^{cr}}{\partial\tilde{q}} = AN\tilde{q}^{N-1}\Delta t \tag{14}$$

For 17-4PH, the austenitization occurs during the heating up process when the temperature is above the starting temperature of austenitization A_{C1}, and martensite

RIGHTSLINK

15512916, 0, Downloaded from https://ceramics.onlinelibrary.wiley.com/doi/10.1111/jace.20190 by Rwth Aachen, Wiley Online Library on [28/10/2024]. See the Terms and Conditions (https://onlinelibrary.wiley.com/terms-and-conditions) on Wiley Online Library for rules of use; OA articles are governed by the applicable Creative Commons License

transformation occurs during cooling down when the temperature drops below the martensite starting temperature M_s.[31] These phase transformations induce volume change ($\Delta\varepsilon^{tr}$ in Equation 5), which influences the deformation or shrinkage of the 17-4PH component. In this aspect, the phase transformations need to be considered in the modeling. The diffusionless transformation of austenite to martensite during the cooling down can be modeled by a modified Koistinen–Marburger (KM) equation[18,32] where the martensite fraction was calculated by

$$\xi_m(T) = \xi_m^{max}\left[1 - \exp\left\{-\left(\frac{M_s - T}{b_m}\right)^{n_m}\right\}\right] \quad (15)$$

where ξ_m^{max} is the maximum volume fraction of martensite after the whole sintering process, M_s is the martensite start temperature, b_m and n_m are two fitting parameters to describe the martensite phase transformation process. These two fitting parameters can be obtained by fitting the Koistinen–Marburger equation to the phase fraction of martensite fraction $\xi_m(T)$ determined from the thermal strain curve measured by dilatometer based on the linear rule of mixture.

During the heating up, austenitization of 17-4PH occurs. In spite of the fact that the austenitization belongs to the group of diffusion-controlled transformation rather than diffusionless transformation, the Koistinen–Marburger equation was still used to describe this process for simplicity reasons. During the heating up phase, the fraction of austenite above A_{C1} temperature was calculated by[32]

$$\xi_a(T) = \xi_a^{max}\left[1 - \exp\left\{-\left(\frac{T - M_a}{b_a}\right)^{n_a}\right\}\right] \quad (16)$$

where ξ_a^{max} is the maximum volume fraction of austenite that is the one after complete austenitization, M_a is the start temperature of austenitization that is commonly named A_{C1} in the phase diagram, and b_a and n_a are two fitting parameters to describe the austenitization process. Similar to the martensite transformation, Equation (16) was used to fit the phase fraction obtained from the thermal strain curve measured by dilatometer during heating up. The fraction of phases as well as the fraction increment of each phase were written in Abaqus subroutine USDFLD.

Phase transformation is usually accompanied by a volume change named as the transformation strain ε_{ij}^{tr}. The thermal strain ε_{ij}^{th} and transformation strain ε_{ij}^{tr} together form the thermo-metallurgical strain ε_{ij}^{thr}, as described in Equation (17). That indicates the strain curve measured by the dilatometer is divided into the thermal strain and the volume change of each phase.

$$\varepsilon_{ij}^{thr}(t) = \delta_{ij}\,\varepsilon_{ij}^{th}(t) + \delta_{ij}\varepsilon_{ij}^{tr}(t) = \delta_{ij}\sum_{k=1}^{2}\varepsilon_k^{th}[T(t)]\,\xi_k(t) \quad (17)$$

where k either equals 1 or 2 indicating austenite (a) or martensite (m). A derivative of Equation (17) yields the increment of thermo-metallurgical strain ε_{ij}^{thr}, which is required for the implementation in Abaqus.

$$\Delta\varepsilon_{ij}^{thr}(t+\Delta t) = \underbrace{\Delta T\delta_{ij}\sum_{k=1}^{2}\alpha_k[T(t+\Delta t)]\xi_k(t)}_{\Delta\varepsilon_{ij}^{th}(t+\Delta t)} + \underbrace{\delta_{ij}\sum_{k=1}^{2}\varepsilon_k^{th}[T(t)]\Delta\xi_k(t+\Delta t)}_{\Delta\varepsilon_{ij}^{tr}(t+\Delta t)} \quad (18)$$

where $\alpha_k = \frac{\Delta\varepsilon_k^{th}}{\Delta T}$ is the first derivative of the thermal strain (or physical CTE) of each phase, ξ_k and $\Delta\xi_k$ the fraction and fraction increment of each phase, δ_{ij} is the Kronecker delta. Phase transformation induced volume changes, and the phase-dependent thermal expansions were implemented using the user-defined subroutine UEXPAN in Abaqus. In addition to phase transformation and transformation-induced volume change, transformation-induced plasticity is another important phenomenon that must be considered in order to predict the residual stresses from the perspective of simulation. The equation proposed by Leblond et al.[33] was used to obtain the increment of the strain component of transformation plasticity:

$$\Delta\,\varepsilon_{ij}^{tp} = -\frac{3}{2}KS_{ij}\ln\xi_m\cdot\Delta\xi_m \quad (19)$$

where K is the coefficient of the transformation plasticity strain. This coefficient was obtained after performing the compression tests at different stress levels during the martensite transformation process with DIL805. The dependence of the transformation plasticity strain on the applied stress levels yields the value of the coefficient K. S_{ij} is the deviatoric stress tensor. The transformation plasticity strain of the metal component was included in the Abaqus subroutine UEXPAN by defining an anisotropic expansion component.

2.4 | Modeling of delamination

For the modeling of delamination, a cohesive element for the mixed interlayer was applied. The strength of the cohesive element determines the damage initiation along

RIGHTSLINK

15512916, 0, Downloaded from https://ceramics.onlinelibrary.wiley.com/doi/10.1111/jace.20190 by Rwth Aachen, Wiley Online Library on [28/10/2024]. See the Terms and Conditions (https://onlinelibrary.wiley.com/terms-and-conditions) on Wiley Online Library for rules of use; OA articles are governed by the applicable Creative Commons License

the interface, whereas the critical strain energy release rate determines the damage evolution and eventually the occurrence of delamination. Damage is assumed to initiate when the maximum nominal stress ratio reaches 1, which can be represented as[34]

$$\max\left\{\frac{\langle t_n\rangle}{\sigma_0}, \frac{t_s}{S}, \frac{t_t}{S}\right\} = 1 \tag{20}$$

where t_n, t_s, and t_t are the stresses in normal and two shear directions, whereas σ_0 and S are the strength in normal and shear direction, respectively. In principle, when the stresses (or traction) reach the strength of the cohesive element in one direction, damage is initialized. Further separation leads to damage evolution, which was simulated using the critical strain energy release rate G_C with a unit of J/m^2, which is related to the energy dissipated per unit area because of the damage process. This value corresponds to the area under the traction–separation curve. In Abaqus, G_C of a cohesive element for the mixed interlayer was specified and a linear softening behavior after damage initiation was assumed. In addition, a damage parameter D_{coh} was used to indicate the damage evolution of the cohesive element, which is defined as[20]

$$D_{coh} = \frac{\delta_f(\delta_{max} - \delta_c)}{\delta_{max}(\delta_f - \delta_c)};\ \ \delta_f = \frac{2G_C}{\sigma_0} \tag{21}$$

where δ_c is the critical displacement when damage initiates, δ_f the displacement at failure, and δ_{max} the maximum displacement attained during the loading history. When δ_{max} reaches δ_f, D_{coh} is 1, representing a complete damage of the cohesive element and the corresponding element will be deleted from the simulation.

3 | RESULTS AND DISCUSSION

3.1 | Input parameters for modeling

Table 1 lists the input parameters for the modeling of densification for 3Y-TZP and 17-4PH. The parameters for viscosity A_0, Q_η, and m_2 in Equation (7) of 3Y-TZP were obtained by fitting its uniaxial viscosity measured in our previous work.[24] Meanwhile, these parameters of 17-4PH were obtained by fitting its relative densities in terms of holding time at different sintering temperatures. For both materials, the grain sizes at different relative densities were used to determine the parameters for grain growth k and n in Equation (11). All required parameters for the modeling of densification are summarized in Table 1.

Besides densification, the thermal strain curve of 17-4PH was used to determine the fraction of austenite and martensite during austenitization while heating up and during the martensite transformation below M_s of cooling down, respectively. The fraction evolution of austenite during heating was obtained based on the linear mixing rule: as introduced in Section 2.3, the modified Koistinen–Marburger equation (Equation 16) was used to fit the fraction evolution of austenite during heating. After fitting, the three parameters M_a, b_a, n_a were obtained to be 658.6°C, 66.5, 1.93 for the modeling of austenitization during heating. Equation (15) was used to fit this temperature-dependent martensite evolution where the three parameters M_s, b_m, n_m were determined to be 222.9°C, 46.6, 2.36 for the modeling of martensitic transformation below the martensite start temperature M_s.

In addition to the phase evolution, the coefficient of transformation plasticity K for Equation (19) was obtained by a linear least-squares fit. Leblond et al.[33] reported the experimentally determined K value for martensitic transformation ranged from 4.5×10^5 to 10^{-4} MPa^{-1}. Deng and Murakawa[36] listed the K value of SUS630 (same as 17-4PH between 8.56×10^{-5} and 9.0×10^{-5} MPa^{-1}. The obtained K value 6.741×10^{-5} MPa^{-1} in this work is in the same order of the values from literature.

3.2 | Relative density gradient and anisotropic sintering shrinkage of single steel tape

During the sintering process of a single steel tape, nontrivial and undesired curvature occurs. This curvature results from an inhomogeneous relative density distribution due to sedimentation of the 17-4PH powder during the tape casting process. This inhomogeneous distribution of the relative density leads to an anisotropic sintering shrinkage, and may eventually be responsible for the undesired deformation or even delamination of composite laminates. As the sintering shrinkage depends simultaneously on the viscosity, the grain size, and the sintering stress, all of which rely on the relative density, it is indispensable to consider the relative density gradient of single steel tape in the FE simulation.

As shown in Figure 3A,B, the distribution of powder (white area) can be clearly observed in an example of a *XY* and *YZ* cross-section after debinding and subsequent pre-sintering until 1000°C. The pre-sintering was performed to obtain some strength of the tape for the preparation process, as the tape direct after debinding is too weak to be prepared for the observation of the cross-section. The relative density distribution on the *XZ* and *YZ* cross-section of a single steel tape was determined by image analysis with the help of Matlab software, which converts the grayscale image into a binary image and divides the region of interest into a desired number of small local grids with an

RIGHTSLINK

15512916, 0, Downloaded from https://ceramics.onlinelibrary.wiley.com/doi/10.1111/jace.20190 by Rwth Aachen, Wiley Online Library on [28/10/2024]. See the Terms and Conditions (https://onlinelibrary.wiley.com/terms-and-conditions) on Wiley Online Library for rules of use; OA articles are governed by the applicable Creative Commons License

TABLE 1 Parameters of 3Y-TZP and 17-4PH used for the modeling of densification.

Parameters	Symbol	3Y-TZP	17-4PH	Unit
Initial average relative density	ρ_0	0.490	0.609	[−]
Material parameter for viscosity	A_0	0.225	0.004	[MPa · s · mm$^{-m_2}$]
Grain growth exponent for viscosity	m_2	2.82	3.0	[−]
Activation energy of deformation	Q_η	514.0[24]	348.5	[kJ/mol]
Parameter related to dihedral angle	α	4.57[24]	4.57	[−]
Arameters for grain growth	k	1.05×10^{-6}	9.76×10^{-3}	[mm^2]
	n	2.76	2.72	[−]
Surface energy	γ	0.3[26]	2.0[35]	[J/m^2]
	N_1	4	3	[−]
Parameters for sintering stress	ζ	0.3	0.2	[−]

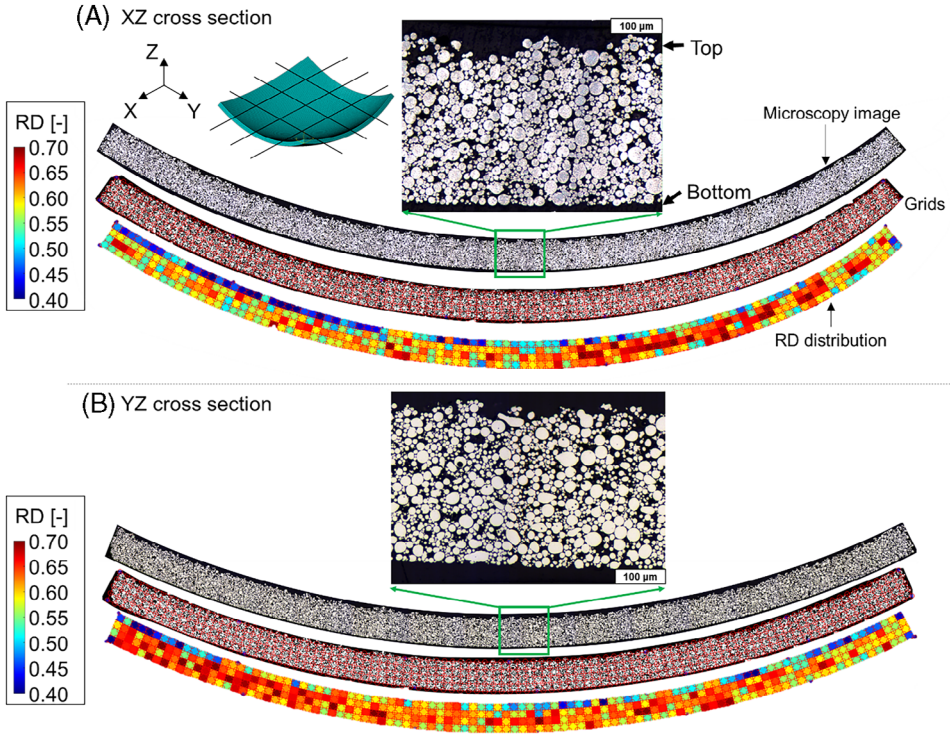


FIGURE 3 Optical microscopy images of cross-sections (top), pre-defined grids of images (middle) and image analysis by Matlab (bottom) to obtain the local relative densities on (A) *XZ* and (B) *YZ* plane for a single 17-4PH tape after debinding with 5 K/min to 250°C and 2 K/min to 500°C, followed by pre-sintering until 1000°C.

identical area. Each cross-section of single steel tape was divided into 4 × 100 grids or local areas. The local relative density was then obtained by calculating the fraction of the white pixel area over the local area.

The inhomogeneous relative density of the steel tape ranging from 0.4 to 0.7 is additionally shown in Figure 3A,B, where the upper layer has a lower relative density than the three bottom layers. The lowest and largest average relative densities of all layers were always found, respectively, at the first (0.494 on the *XZ* plane and 0.568 on the *YZ* plane) and third layers (0.569 on the *XZ* plane and 0.629 on the *YZ* plane) with an absolute difference of approximately 7%. This mainly results from the sedimentation of steel powder, and leads to the curvature of a single steel tape during sintering in the positive *Z* direction. It is also interesting to see that the third layer rather than the bottom layer has the largest relative density. It is believed that the chemical composition and viscosity of binder play a role here. In addition, along the casting direction *X*, the average relative density 0.543 on the *XZ* plane is lower than 0.606 on the *YZ* plane. This can probably be explained by the fact that during the tape

15512916, 0, Downloaded from https://ceramics.onlinelibrary.wiley.com/doi/10.1111/jace.20190 by Rwth Aachen, Wiley Online Library on [28/10/2024]. See the Terms and Conditions (https://onlinelibrary.wiley.com/terms-and-conditions) on Wiley Online Library for rules of use; OA articles are governed by the applicable Creative Commons License

RIGHTSLINK

casting process, the doctor blade spreads the steel powder along the casting direction *X*, leading to a larger distance between adjacent powders, and therefore, lower relative density on the *XZ* plane. The average relative density on the *XZ* plane is approximately 6% lower than that on the *YZ* plane. This results in a larger curvature during sintering on the *XZ* plane than on the *YZ* plane.

To obtain a more representative relative density distribution of a single steel tape, three cross-sections on each *XZ* and *YZ* plane were analyzed. Each local relative density was obtained by averaging six measured relative densities at the corresponding coordinate location. For instance, the local relative density at coordinates $(X,Y,Z) = (1,1,1)$ is obtained by averaging the three local relative densities measured at (1,:,1) from the *XZ* plane and the other three local relative densities measured at (:,1,1) from the *YZ* plane. To this end, a number set of $100 \times 100 \times 4$ local relative densities with their corresponding coordinates were obtained. As the total average relative density of these 40 000 values is 0.576, which is lower than the measured relative green density 0.609 of single steel tape, a correction factor of 1.057 was used to multiply the 40 000 local relative densities. Subsequently, these 40 000 local relative densities were successfully mapped to the corresponding 40 000 C3D8T elements in Abaqus, as illustrated in Figure 4A. It is clear that an inhomogeneous relative density distribution with lower relative densities of the upper layer was obtained.

After carrying out the FE sintering simulation, the deformation and displacement along the *Z* direction of a single steel tape are shown in Figure 4B. As expected, the steel tape bends in the positive *Z* direction due to the lower relative density of the upper layers. Moreover, it bends to a higher extent in the casting direction (*XZ* plane) than the perpendicular direction (*YZ* plane). These two observations correspond very well to the experimental results. Figure 4C plots the curvature evolution on the *XZ* and *YZ* planes during the entire sintering process based on FE simulation. If not explained otherwise, the curvatures in this work are always measured on the middle *XZ* and *YZ* cross-section. When the temperature reaches approximately 1050°C, the single steel tape starts to bend, and the bending accelerates with higher temperature on both planes. At 1225°C, the curvature on the *XZ* plane exceeds the *YZ* plane. The eventual curvature on the *XZ* plane is approximately 1.53 times of that on the *YZ* plane, clearly indicating an anisotropic sintering of single steel tape due to the relative density gradient induced by tape casting process.

Besides, the curvature of a single steel tape after sintering was calculated after obtaining 3D geometry of the specimen by GOM (Gesellschaft für Optische Messtechnik) measurement, as shown in Figure 4C. While the simulation-predicted curvature on the *XZ* plane corresponds to the measured value very well (with a difference of only 3.8%), the curvature on the *YZ* plane is 25% more than the experimental value. Analysis of an insufficient number of cross-sections may account for the difference. A more precise capture, for example, by CT (computed tomography) scan of the initial relative density distribution should be considered in the future. With the developed method, the inhomogeneous relative density distribution of the steel tape can be taken into account in the sintering model, whereby the simulation successfully predicts the bending and anisotropic sintering shrinkage to a reasonable extent.

3.3 | Sintering shrinkage and deformation of asymmetric laminates (m-m-c and c-c-m)

As a mixed interlayer was added to adjacent tapes with different materials for asymmetric laminates m-m-c and c-c-m (see Figure 2A,B), cohesive elements were used for the modeling of the mixed interlayer. Based on the experimental observation of the m-m-c and the c-c-m laminate, no apparent delamination was found during the co-sintering process. Therefore, an ideal strength of 2 MPa and a critical strain energy release rate of 0.05 mJ/mm^2,[37] were assumed for the cohesive element to model the mixed interlayer in m-m-c and c-c-m.

Figure 5A shows the comparison of the sintering shrinkage and linear shrinkage rate between experimental measurements and simulation results. While the total linear shrinkage of the m-m-c laminate was 16.3% from the dilatometer measurement, a shrinkage of 16.5% was obtained from the simulation. This yields an acceptable difference of +0.2% between experimental and simulation results. In addition, a maximum shrinkage rate of -0.335 min^{-1} was obtained from the dilatometer measurement at 1274°C, whereas the simulation showed a maximum shrinkage rate of -0.348 min^{-1} at 1347°C, which is close to the maximum sintering temperature. The shrinkage rate from simulation followed a different trend from the experiment: it first increased to -0.25 min^{-1} at approximately 1200°C, then decreased to -0.225 min^{-1} at 1245°C, and increased again to the maximum rate of -0.348 min^{-1} at 1347°C. In spite of the different tendency of shrinkage rate, the shrinkage curve as well as the total shrinkage of simulation corresponds well to the experiment. The deformation of the m-m-c laminate is also in good accordance with the experimental silhouettes, as illustrated in Figure 5B. As the mixed interlayer is modeled as cohesive element, the value of relative density for this layer is missing. It is within expectation that the

RIGHTSLINK

15512916, 0, Downloaded from https://ceramics.onlinelibrary.wiley.com/doi/10.1111/jace.20190 by Rwth Aachen, Wiley Online Library on [28/10/2024]. See the Terms and Conditions (https://onlinelibrary.wiley.com/terms-and-conditions) on Wiley Online Library for rules of use; OA articles are governed by the applicable Creative Commons License

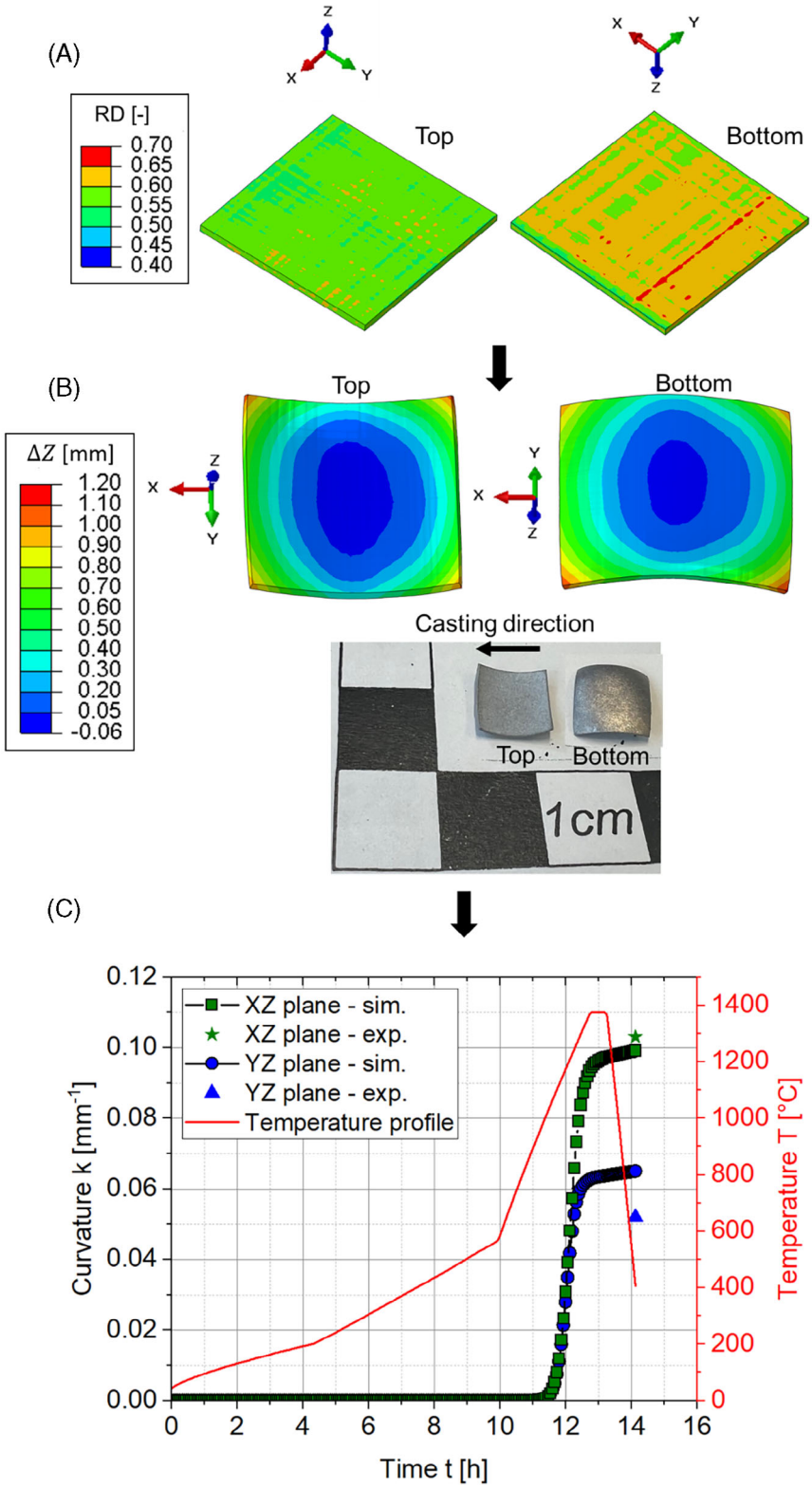


FIGURE 4 (A) Mapping of the local relative densities to the elements in simulation. (B) Deformation of single steel tape after sintering from simulation and experiments. (C) Curvature evolution on the middle *XZ* and *YZ* plane from simulation, and the corresponding measured curvature from single steel tape after sintering.

c-c-m laminate bents toward the side of ceramic tape due to higher shrinkage/rate and Young's modulus of 3Y-TZP at high temperature.

To further validate the developed model, the curvatures of the silhouettes were calculated by Matlab after obtaining the coordinates of three points by an online tool PlotDigitizer.[38] In terms of simulation, the coordinates of three nodes on the *XZ* and *YZ* plane during the whole sintering process were exported. These time-dependent coordinates were used to calculate the curvatures on the

RIGHTSLINK

15512916, 0, Downloaded from https://ceramics.onlinelibrary.wiley.com/doi/10.1111/jace.20190 by Rwth Aachen, Wiley Online Library on [28/10/2024]. See the Terms and Conditions (https://onlinelibrary.wiley.com/terms-and-conditions) on Wiley Online Library for rules of use; OA articles are governed by the applicable Creative Commons License

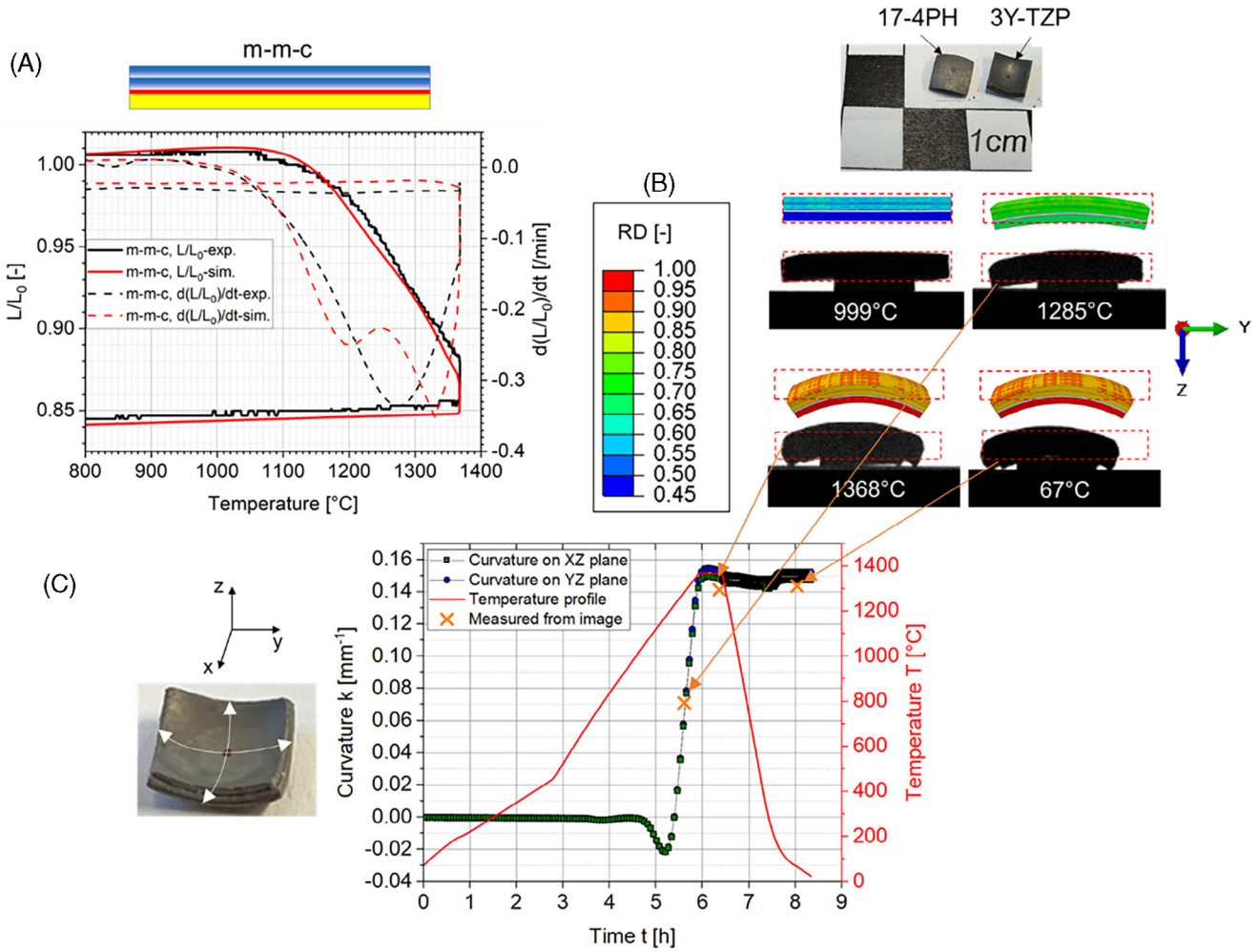


FIGURE 5 (A) Comparison of shrinkage and shrinkage rate of the m-m-c laminate between simulation and experiment. Blue and white represent the bottom and top side with higher and lower relative density of a single 17-4PH tape, respectively. (B) Shape of the m-m-c laminate after sintering and comparison between the deformation in simulation and experimental silhouettes of the m-m-c laminate during sintering. (C) The coordinate system to obtain the curvature, curvature evolution on *XZ* and *YZ* plane, and three measured curvatures from the silhouettes.

XZ and *YZ* plane with respect to time in Matlab, and the results are shown in Figure 5C. The measured curvature from the silhouette at 1285°C were located exactly on the curvature evolution curve of the simulation. Meanwhile, the simulation results of curvatures at 1368°C and 67°C were approximately 6% higher than those measured from the silhouettes. All these comparisons validate the accuracy of the developed model applied in the simulation.

It is also interesting to observe that at the temperature range of approximately 1000°C–1100°C, the curvature is negative, which indicates the m-m-c laminate first bents toward the side of 17-4PH. This results from a lower start temperature of shrinkage of 17-4PH (~1000°C) than of 3Y-TZP (~1060°C). As temperature continued to increase, 3Y-TZP shrank faster and pulled the whole structure to bend toward the ceramic side. In addition, the anisotropic shrinkage was significantly reduced due to the dominant role of 3Y-TZP, which shrank isotropically during sintering. According to the simulation result, the width changes on the *XZ* (17.0%) and *YZ* planes (16.5%) were similar with a minor difference of 0.5%. Interestingly, in spite of a 0.5% larger shrinkage on the *XZ* plane than the *YZ* plane, the final curvature on the *XZ* plane (0.148 mm^{-1}) was lower than that on the *YZ* plane (0.152 mm^{-1}). This observation was unexpected, as the curvature of single steel tape on the *XZ* plane (casting direction) was almost double of that on the *YZ* plane (see Figure 4C). Moreover, the influence of austenitization starting at approximately 660°C and martensite transformation starting at approximately 220°C on the deformation can be spotted from the curves of the curvature evolution. Especially for the martensite transformation, the approximately 4.6% volume increase[39] of steel tape pulls the ceramic tapes, leading to a larger curvature of the laminate.

RIGHTSLINK
15512916, 0, Downloaded from https://ceramics.onlinelibrary.wiley.com/doi/10.1111/jace.20190 by Rwth Aachen, Wiley Online Library on [28/10/2024]. See the Terms and Conditions (https://onlinelibrary.wiley.com/terms-and-conditions) on Wiley Online Library for rules of use; OA articles are governed by the applicable Creative Commons License

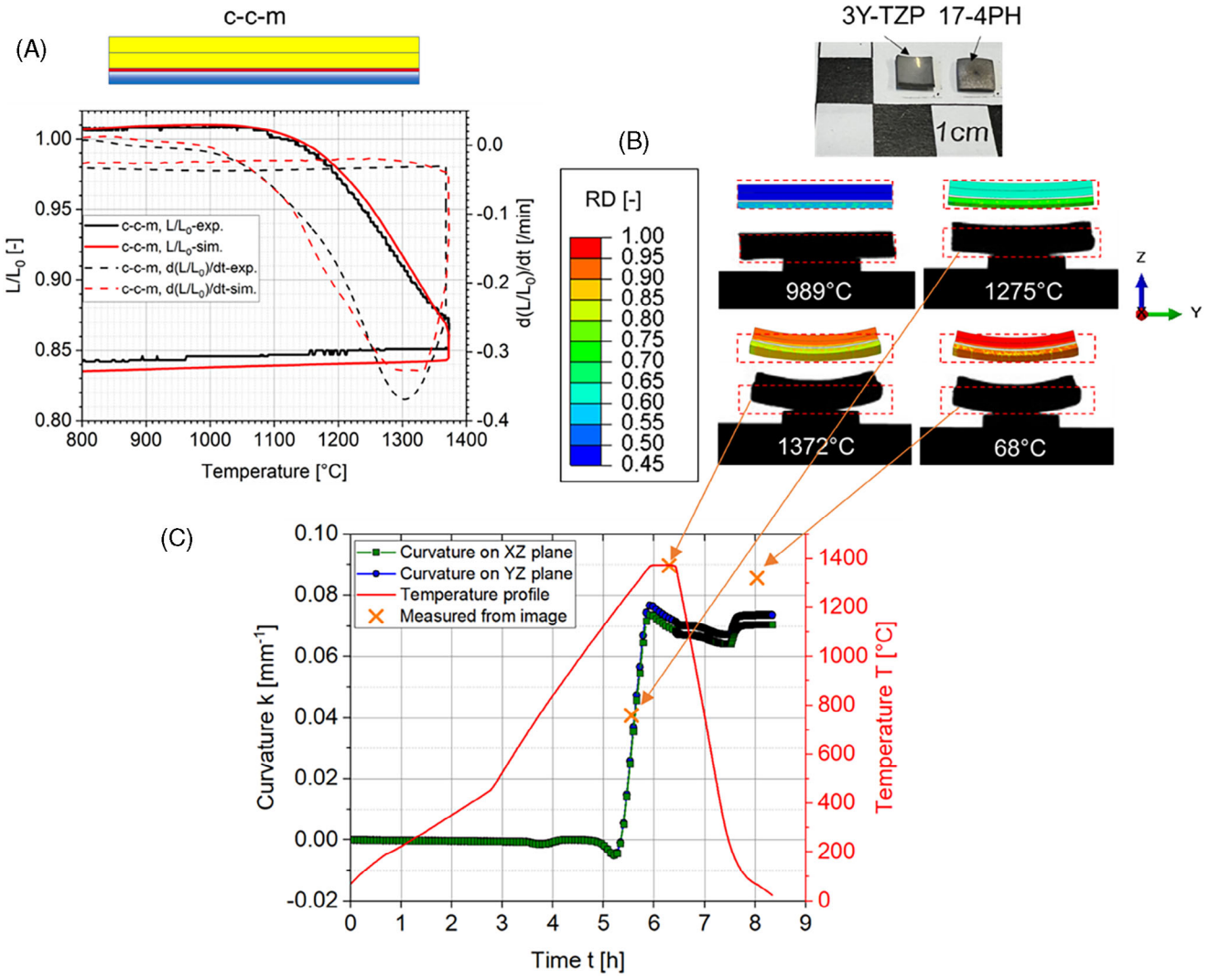


FIGURE 6 (A) Comparison of shrinkage and shrinkage rate of the c-c-m laminate between simulation and experiment. (B) Shape of the c-c-m laminate after sintering and comparison between the deformation in simulation and experimental silhouettes of the c-c-m laminate during sintering. (C) Curvature evolution on the *XZ* and *YZ* plane from simulation and three measured curvatures from the silhouettes.

The developed model was further applied to the c-c-m laminate. As shown in Figure 6A, the width change (shrinkage) from the simulation is in good accordance with the dilatometer measurement. The total shrinkage of the simulation is 17%, 0.3% larger than the experimental result. In addition, the shrinkage rate curve of the simulation follows similar trend of the experimental data. The maximum shrinkage rate $-0.327\ \text{min}^{-1}$ of simulation is approximately 11% less than the experimental result of $-0.367\ \text{min}^{-1}$. Both occurred at approximately 1300°C. The comparison between the deformation in simulation and experimental silhouettes of the c-c-m laminate is shown in Figure 6B. In general, the c-c-m laminate is bent toward the ceramic side. The curvature increased as the sintering proceeded. In order to quantitatively compare the curvature evolution from simulation and experiment, the same method that had been used for the m-m-c laminate was applied to the c-c-m laminate, as shown in Figure 6C. It is clear that the final curvature of c-c-m ($0.086\ \text{mm}^{-1}$) calculated from the image is significantly lower than that of m-m-c ($0.144\ \text{mm}^{-1}$). This can be explained by the fact that the ceramic tape is thicker than the steel tape and much stiffer at high temperatures. The existence of two 3Y-TZP tapes in c-c-m laminate led to less deformation and curvature.

Similar to the simulation results in the m-m-c laminate, the final curvature of the c-c-m laminate on the *YZ* plane ($0.735\ \text{mm}^{-1}$) is slightly larger than that on the *XZ* plane ($0.705\ \text{mm}^{-1}$, casting direction), in spite of a lower total shrinkage on the *YZ* plane (18.4%) than on the *XZ* plane (18.7%). Again, the anisotropic sintering shrinkage of the c-c-m laminate was significantly reduced due to the isotropic shrinkage of the 3Y-TZP tape. The curvature obtained from the simulation ($0.0735\ \text{mm}^{-1}$) underestimated the

RIGHTSLINK

15512916, 0, Downloaded from https://ceramics.onlinelibrary.wiley.com/doi/10.1111/jace.20190 by Rwth Aachen, Wiley Online Library on [28/10/2024]. See the Terms and Conditions (https://onlinelibrary.wiley.com/terms-and-conditions) on Wiley Online Library for rules of use; OA articles are governed by the applicable Creative Commons License

final curvature (0.0857 mm^{-1}) measured from the silhouettes by approximately 14%. A multitude of reasons could explain this difference. For instance, uncertainties may occur when capturing the coordinates by the online tool PlotDigitizer. Besides, the simulation always uses the same relative density distribution of steel tape in Section 3.2. Nevertheless, the actual relative density distribution in the experiment may vary from one steel tape to another. This may also lead to the underestimation of curvature in c-c-m.

3.4 | Sintering shrinkage and deformation of symmetric laminates (c-m-c and m-c-m)

The apparent delamination was found in symmetric laminates rather than asymmetric laminates, as shown in Figures 7B and 8B. In addition, delamination always occurs at the mixed interlayer between metal and ceramic tape. One critical difference between symmetric and asymmetric laminates is that the symmetric laminates have two mixed interlayers instead of one. In the scenario of c-m-c, the upper 3Y-TZP tape pulls the middle 17-4PH tape upwards (due to higher shrinkage of 3Y-TZP than 17-4PH) and the lower 3Y-TZP tape pulls it downwards. The stresses cannot be reduced by bending. Delamination begins from the edges where the highest stresses are expected. At the top, debinding could take place relatively easily via the free surface. At the bottom, it is hindered by the support. This may result in a stronger upper mixed interlayer than the bottom one in symmetric laminates. Based on this assumption, the critical strain energy release rate of cohesive elements to model the delamination of the upper and lower mixed interlayer were selected to be 0.05 and 0.011 mJ/mm^2, respectively.

Similar to the analysis of the other laminates, Figure 7A compares the linear sintering shrinkage and shrinkage rate between the simulation results and the dilatometer measurement. From the experiment, a total shrinkage of 18.7% was obtained, while the simulation result showed a total shrinkage of 18.8%, which is 0.1% larger than the experimental result. The shrinkage rate curve indicated that upon the beginning of sintering (densification), the simulation predicted a lower shrinkage rate than the experimental result. Nevertheless, at the temperature range of 1150°C–1365°C, the shrinkage rate predicted from the simulation exceeded that obtained from the experiment. While the maximum shrinkage rate of c-m-c from the simulation was $-0.358\ min^{-1}$ at 1260°C, it reached $-0.297\ min^{-1}$ at 1272°C from experimental measurements. The predicted maximum shrinkage rate from the simulation is 15.4% higher than that from the experiment. Nonetheless, the lower shrinkage rate of the simulation at temperatures below 1150°C and above 1365°C averaged the higher shrinkage rate, resulting in only 0.1% larger total shrinkage in comparison to experimental results.

The shrinkage (densification), deformation, and delamination of c-m-c are visualized by silhouettes in Figure 7B. No clear delamination was observed until 1303°C. Then the delamination of the lower mixed interlayer started to occur at the four corners. Once delamination occurred, further densification of the ceramic tape bent the edges away from the center, as can be observed from the silhouettes at 1368°C. Subsequent cooling seems not lead to further significant delamination. The layers are still well connected in the middle of the c-m-c laminate after sintering.

To figure out the procedure of the delamination process, the evolution of thermal strains of 3Y-TZP and 17-4PH obtained from simulation are plotted in Figure 7C, where several typical temperatures were selected for the analysis. The damage parameters D_{coh} (see Equation 21) along the mixed interlayer at these selected temperatures is plotted in Figure 7D. Upon the start of austenitization at 698°C, damage was already initiated mainly due to the assumed low strength (2 MPa) of the cohesive elements. At the end of the austenitization process, D_{coh} of all cohesive elements are above 0.95. This indicates an apparent effect of the austenitization process on delamination when the strength of the mixed interlayer is too low. This resulted from a larger gap of thermal strains between 17-4PH and 3Y-TZP as austenitization proceeded. At 911°C, D_{coh} of several cohesive elements near the corner approached 1, but not yet reached 1 as the cohesive elements were not deleted. At 1303°C, delamination is detected and propagated slightly during the holding period. During the cooling phase, 17-4PH shrinks faster than 3Y-TZP due to the higher thermal expansion coefficient of steel in comparison to ceramic, leading to further delamination as shown at 800°C. The volume increase of 17-4PH due to martensite transformation led to a complete delamination of edges as shown at 68°C.

A first glance at the sintered m-c-m laminate in Figure 8B implies that gravity seems to play a non-negligible role during the sintering process, as this laminate is bent toward the ground. However, this assumption is probably unreasonable, as viscosity and Young's modulus of the 3Y-TZP component are high even at temperature above 1300°C. This means that the middle ceramic tape will prevent the whole laminate from bending to a large extent in spite of the fact that the steel layer is very soft at such high temperature. In addition, the laminate size is so small that gravity is unlikely to distort the laminate to an extent as observed from the silhouettes captured by the optical dilatometry. Instead, a more reasonable process would be that delamination already occurs between top steel tape and middle ceramic tape at temperature above

RIGHTSLINK

15512916, 0, Downloaded from https://ceramics.onlinelibrary.wiley.com/doi/10.1111/jace.20190 by Rwth Aachen, Wiley Online Library on [28/10/2024]. See the Terms and Conditions (https://onlinelibrary.wiley.com/terms-and-conditions) on Wiley Online Library for rules of use; OA articles are governed by the applicable Creative Commons License

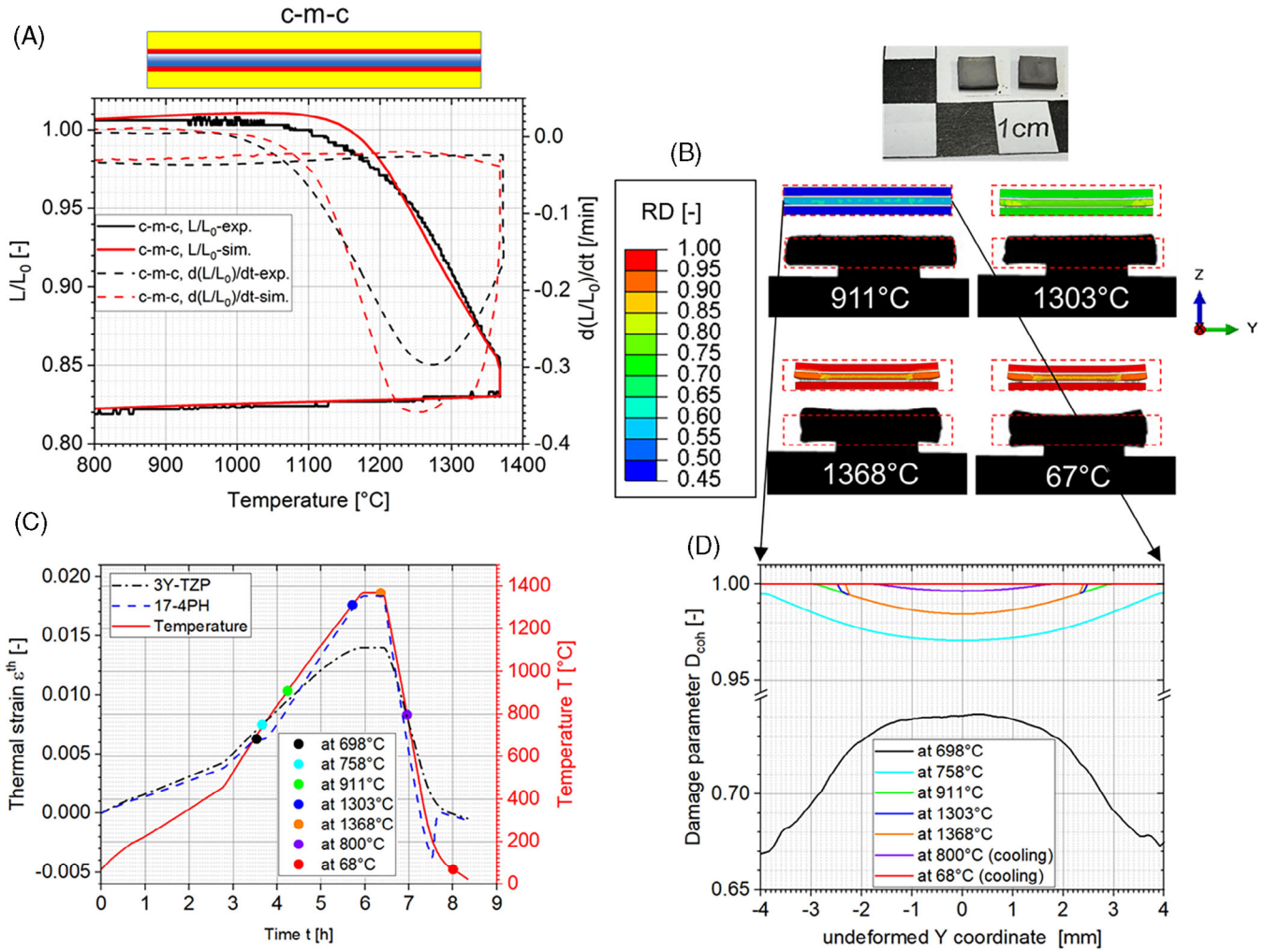


FIGURE 7 (A) Comparison of shrinkage and shrinkage rate of the c-m-c laminate between simulation and experiment. (B) Shape of the c-m-c laminate after sintering and comparison between the deformation in simulation and experimental silhouettes of the c-m-c laminate during sintering. (C) Thermal strain curve of 3Y-TZP and 17-4PH during co-sintering process and several selected temperatures to study the delamination propagation of the c-m-c laminate. (D) The damage parameters of the cohesive elements along the outer edge of the bottom mixed interlayer in the c-m-c laminate.

971°C. As the middle ceramic tape has a large shrinkage rate, it pulls the top steel tape together downwards. As the steel component is much softer, the bottom steel tape was "forced" to be bent toward the ground at the same time.

The shrinkage and shrinkage rate predicted by simulation generally overestimated the values compared to those obtained experimentally, as shown in Figure 8A. The total shrinkage obtained from the simulation was 18.1%, which is 1.7% larger than that obtained from the experiment. Meanwhile, the maximum shrinkage rate in the simulation was more than 30% larger than experimentally determined. It should be noted that the FE simulation of m-c-m did not consider the contact issue between the middle 3Y-TZP tape and the bottom 17-4PH tape after delamination. The middle 3Y-TZP tape penetrated into the bottom 17-4PH tape in the simulation, which did not occur in experiments where the middle 3Y-TZP took the top and bottom 17-4PH tape to bend to a higher curvature than in the simulation.

The delamination process was analyzed using the same method applied to the c-m-c laminate. The selected temperatures are shown in Figure 8C. Again, it is observed that under the current assumptions for the strength and critical energy release rate of the cohesive elements used to simulate the delamination of mixed interlayers, austenitization contributed significantly to the delamination process. As shown in Figure 8D, at temperatures above 971°C up to the maximum temperature, delamination propagated very slowly, as the shear stresses at such high temperatures are completely relaxed. During cooling, delamination further proceeds due to a large difference in thermal strains of two materials as well as the martensite

15512916, 0, Downloaded from https://ceramics.onlinelibrary.wiley.com/doi/10.1111/jace.20190 by Rwth Aachen, Wiley Online Library on [28/10/2024]. See the Terms and Conditions (https://onlinelibrary.wiley.com/terms-and-conditions) on Wiley Online Library for rules of use; OA articles are governed by the applicable Creative Commons License

RIGHTSLINK

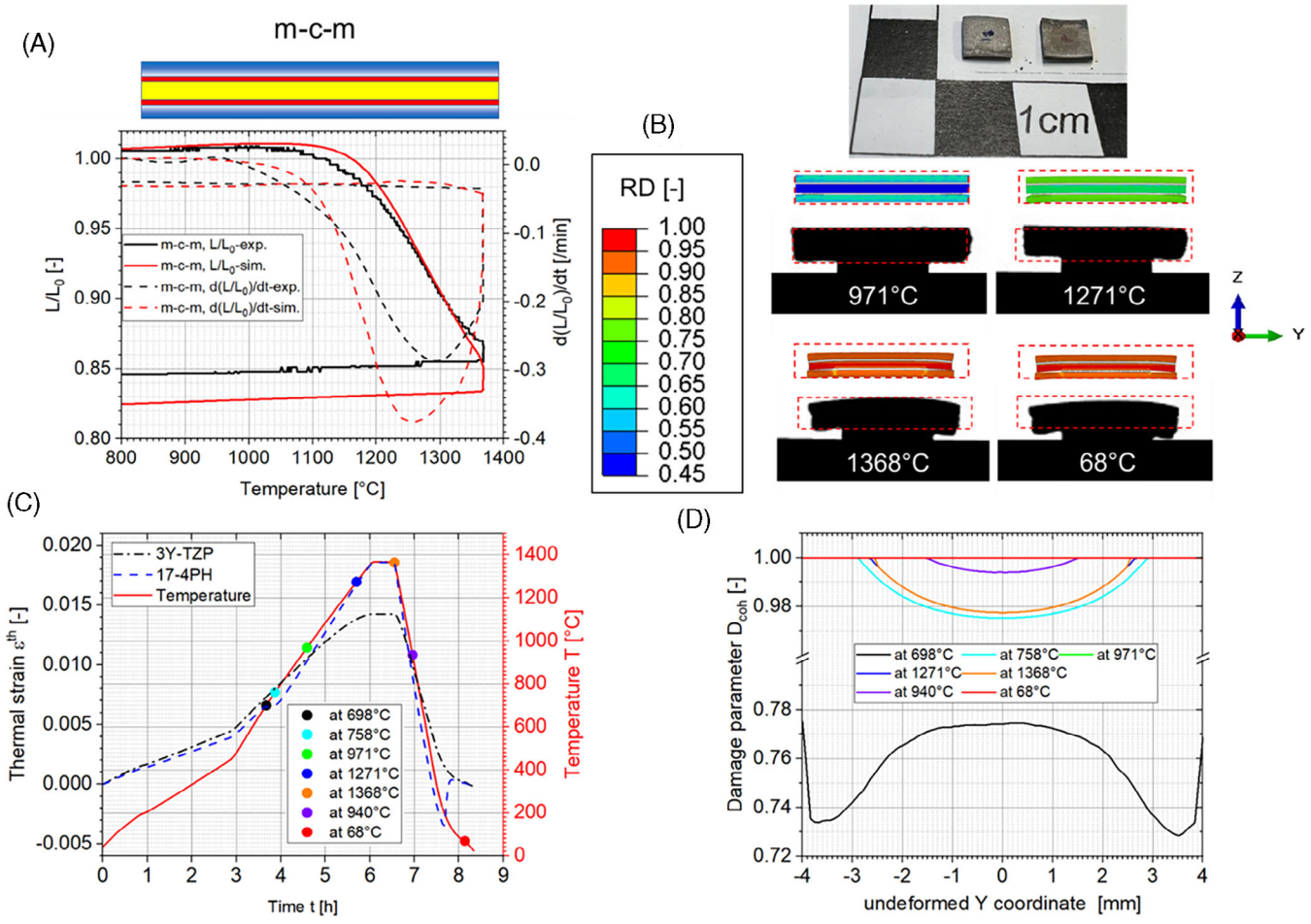


FIGURE 8 (A) Comparison of shrinkage and shrinkage rate of the m-c-m laminate between simulation and experiment. (B) Shape of the m-c-m laminate after sintering and comparison between the deformation in simulation and experimental silhouettes of the m-c-m laminate during sintering. (C) Thermal strain curve of 3Y-TZP and 17-4PH during co-sintering process and several selected temperatures to study the delamination propagation in the m-c-m laminate. (D) The damage parameters of cohesive elements along the outer edge of the bottom mixed interlayer in the m-c-m laminate.

TABLE 2 Comparison of the total shrinkage from experiment and simulation for all investigated laminates.

Laminates	Experiment Total shrinkage in %	Simulation Total shrinkage in %	Difference in %
m-m-c	16.3	16.5	0.2
c-c-m	16.7	17.0	0.3
c-m-c	18.7	18.8	0.1
m-c-m	16.4	18.1	1.7

transformation-induced volume increase. A complete delamination at the edges was obtained in the simulation. This is in good accordance with the experimental observations for the m-c-m laminate.

To summarize, delamination in symmetric laminates mainly results from a combination effect of worse debinding at the bottom mixed interlayer and a large difference of the thermal strains of the two materials at low temperature due to phase transformation. By assuming a lower critical strain energy release rate of cohesive elements for the modeling of the bottom mixed interlayers, similar deformation and delamination process as observed in the experiment for symmetric laminates were achieved. Based on the simulation, the cohesive elements need to have more than 0.05 mJ/mm^2 in order to avoid complete delamination.

Table 2 lists the total shrinkage values for all laminates investigated experimentally and by simulation. Besides the m-c-m laminate with strong asymmetrical

RIGHTSLINK

15512916, 0, Downloaded from https://ceramics.onlinelibrary.wiley.com/doi/10.1111/jace.20190 by Rwth Aachen, Wiley Online Library on [28/10/2024]. See the Terms and Conditions (https://onlinelibrary.wiley.com/terms-and-conditions) on Wiley Online Library for rules of use; OA articles are governed by the applicable Creative Commons License

delamination problems, the developed thermo-mechanical-metallurgical model is able to predict the total shrinkage of all the other three laminates to a very good extent with a maximum difference of 0.3%. This validates the capability of the developed model.

4 | CONCLUSIONS

- A thermo-mechanical-metallurgical model was successfully developed and applied to investigate the shrinkage, shrinkage rate, deformation, and delamination of metal–ceramic laminates.
- The relative density gradient of a single steel tape, which resulted from sedimentation of 17-4PH powder during tape casting and drying of the tape and led to its anisotropic curvatures, was obtained by image analysis in Matlab, and successfully considered and mapped to the elements of the steel tape in the simulation. The curvatures on the *XZ* and *YZ* planes from the simulation correspond well to those obtained by GOM measurements.
- For asymmetric laminates (m-m-c and c-c-m), no apparent delamination was observed. The ceramic tape dominates the co-sintering process due to its higher shrinkage rate and stiffness compared to the steel tape. The densification, deformation, and curvatures can be predicted by the developed model with high accuracy.
- For symmetric laminates (c-m-c and m-c-m), delamination occurred during the co-sintering process. The simulation results indicated that the bottom mixed interlayer has a lower critical energy release rate, leading to the delamination of middle tape and bottom tape. This could be related to the debinding process. Debinding on the bottom side is more hindered through the support than on the upper side with the free surface. Once the delamination of the lower ceramic–metal interlayer starts, the ceramic tape causes the whole structure to bend toward the ceramic side.
- Phase transformation plays a crucial role in the occurrence of delamination, especially when the interface is weak. As the phase transformation is usually accompanied by a change in volume, larger differences in thermal stresses and thus delamination can occur.

ACKNOWLEDGMENTS

The authors gratefully acknowledge the review and feedback from Dr. Bengt Hallstedt (IWM, RWTH). The authors would like to thank M. Sc. Valérian Iss, Dr. -Ing. Ali Rajaei, and M. Sc. Soheil Rooein (group of heat treatment, IWM, RWTH Aachen) for the fruitful discussions regarding the modeling of phase transformation as well as transformation-induced plasticity. This project was supported by the German Research Foundation (DFG) under the contract number 441616349.

REFERENCES

1. Rödel J, Kounga ABN, Weissenberger-Eibl M, Koch D, Bierwisch A, Rossner W, et al. Development of a roadmap for advanced ceramics: 2010–2025. J Eur Ceram Soc. 2009;29:1549–60.
2. Bermejo R, Llanes L, Anglada M, Supancic P, Lube T. Thermal shock behavior of an Al_2O_3/ZrO_2 multilayered ceramic with residual stresses due to phase transformations. Key Eng Mater. 2005;290:191–98.
3. Abel J, Scheithauer U, Janics T, Hampel S, Cano S, Müller-Köhn A, et al. Fused filament fabrication (FFF) of metal-ceramic components. J Vis Exp. 2019;143:e57693.
4. Scheithauer U, Slawik T, Haderk K, Moritz T, Michaelis A, editors. Development of planar and cylindrical refractories with graded microstructure. Fraunhofer-Publica; 2013.
5. Scheithauer U, Schwarzer E, Otto C, Slawik T, Moritz T. Ceramic and metal-ceramic components with graded microstructure. In: Lin H-T, Hemrick J, editors. Advanced and refractory ceramics for energy conservation and efficiency. Vol. 256. Hoboken, NJ, USA: John Wiley & Sons, Inc; 2016. p. 149–60.
6. Cai PZ, Green DJ, Messing GL. Constrained densification of alumina/zirconia hybrid laminates, I: experimental observations of processing defects. J Am Ceram Soc. 1997;80:1929–39.
7. Largiller G, Bouvard D, Carry CP, Gabriel A, Müller J, Staab T. Deformation and cracking during sintering of bimaterial components processed from ceramic and metal powder mixes. Part I: Experimental investigation. Mech Mater. 2012;53:123–31.
8. Green DJ, Guillon O, Rödel J. Constrained sintering: a delicate balance of scales. J Eur Ceram Soc. 2008;28:1451–66.
9. Dourandish M, Simchi A, Tamjid Shabestary E, Hartwig T. Pressureless sintering of 3Y-TZP/stainless-steel composite layers. J Am Ceram Soc. 2008;91:3493–503.
10. Slawik T, Bergner A, Puschmann R, Franke P, Raethel J, Behnisch T, et al. Metal-ceramic layered materials and composites manufactured using powder techniques. Adv Eng Mater. 2014;16:1293–302.
11. Slawik T, Günther A, Moritz T, Michaelis A. Co-sintering behaviour of zirconia-ferritic steel composites. AIMS Mater Sci. 2016;3:1160–76.
12. Shi H, Giuntini D, van Dommelen H, Geers MG, Remmers JJ. Efficient modeling of ceramic sintering processes: application to bilayers and membranes. J Eur Ceram Soc. 2023;43:4939–49.
13. Largiller G, Dong L, Bouvard D, Carry CP, Gabriel A. Deformation and cracking during sintering of bimaterial components processed from ceramic and metal powder mixes. Part II: Numerical simulation. Mech Mater. 2012;53:132–41.
14. Schoenberg SE, Green DJ, Segall AE, Messing GL, Grader AS, Halleck PM. Stresses and distortion due to green density gradients during densification. J Am Ceram Soc. 2006;89:3027–33.
15. Olevsky EA, Tikare V, Garino T. Multi-scale study of sintering: a review. J Am Ceram Soc. 2006;89:1914–22.
16. Molla TT, Ni DW, Bulatova R, Bjørk R, Bahl C, Pryds N, et al. Finite element modeling of camber evolution during sintering of bilayer structures. J Am Ceram Soc. 2014;97:2965–72.
17. Schmidt I, Kraft T. Simulation of the co-sintering of composite structures. Int J Mat Res. 2010;101:933–41.

RIGHTSLINK

15512916, 0, Downloaded from https://ceramics.onlinelibrary.wiley.com/doi/10.1111/jace.20190 by Rwth Aachen, Wiley Online Library on [28/10/2024]. See the Terms and Conditions (https://onlinelibrary.wiley.com/terms-and-conditions) on Wiley Online Library for rules of use; OA articles are governed by the applicable Creative Commons License

18. Eser A, Broeckmann C, Simsir C. Multiscale modeling of tempering of AISI H13 hot-work tool steel—part 2: coupling predicted mechanical properties with FEM simulations. Comput Mater Sci. 2016;113:292–300.
19. Lu X, Ridha M, Chen BY, Tan V, Tay TE. On cohesive element parameters and delamination modeling. Eng Fract Mech. 2019;206:278–96.
20. Camanho PP, Davila CG, De Moura MF. Numerical simulation of mixed-mode progressive delamination in composite materials. J Compos Mater. 2003;37:1415–38.
21. Günther A, Moritz T, Mühle U. Microstructure and interface characteristics of 17-4PH/YSZ components after co-sintering and hydrothermal corrosion. Ceramics. 2020;3:245–57.
22. Riedel H, Kozák V, Svoboda J. Densification and creep in the final stage of sintering. Acta Metall Mater. 1994;42:3093–103.
23. Rahaman MN, Sintering of ceramics. CRC Press; 2007.
24. Liu C, Herrmann M, Deng Y, Kaletsch A, Broeckmann C. Analysis of uniaxial viscosity and activation energy of deformation for 3Y-TZP by bending creep test. Ceram Int. 2023;49:22806–15.
25. Bordia RK, Scherer GW. On constrained sintering—I. Constitutive model for a sintering body. Acta Metall. 1988;36:2393–97.
26. Kwon Y-S, Wu Y, Suri P, German RM. Simulation of the sintering densification and shrinkage behavior of powder-injection-molded 17-4 PH stainless steel. Metall Mater Trans A. 2004;35:257–63.
27. Shinagawa K. Micromechanical modeling of viscous sintering and a constitutive equation with sintering stress. Comput Mater Sci. 1999;13:276–85.
28. McMeeking RM, Kuhn LT. A diffusional creep law for powder compacts. Acta Metall Mater. 1992;40:961–69.
29. Beiss P. Pulvermetallurgische Fertigungstechnik. Berlin, Heidelberg: Springer Berlin Heidelberg; 2013.
30. Balshin MY. Relation of mechanical properties of powder metals and their porosity and the ultimate properties of porous metal–ceramic materials. Dokl Akad Nauk SSSR. 1949;67;831–34.
31. Liu C, Günther A, Deng Y, Kaletsch A, Herrmann M, Broeckmann C. Investigation on the curvature and stress distribution of laminates based on an analytic solution and FE simulation. Materials (Basel). 2022;15:6458.
32. Koistinen DP, Marburger RE. A general equation prescribing the extent of the austenite-martensite transformation in pure iron-carbon alloys and plain carbon steels. Acta Metall. 1959;7:59–60.
33. Leblond JB, Devaux J, Devaux JC. Mathematical modeling of transformation plasticity in steels I: case of ideal-plastic phases. Int J Plast. 1989;5:551–72.
34. Systèmes D. Abaqus analysis user's manual. Providence, RI, USA: Simulia Corp.; 2007. p. 40.
35. German RM. Sintering theory and practice. Hoboken, NJ: Wiley-Interscience; 1994.
36. Deng D, Murakawa H. Influence of transformation induced plasticity on simulated results of welding residual stress in low temperature transformation steel. Comput Mater Sci. 2013;78:55–62.
37. Evans AG, Hutchinson JW. The thermomechanical integrity of thin films and multilayers. Acta Metall Mater. 1995;43:2507–30.
38. PlotDigitizer: extract data from graph image online. PlotDigitizer. Accessed October 11, 2023. https://plotdigitizer.com/
39. Ericsson T. Residual stresses produced by quenching of martensitic steels. In: Comprehensive materials processing. Amsterdam: Elsevier; 2014. p. 271–98.

How to cite this article: Liu C, Deng Y, Gruner D, Kaletsch A, Gestrich T, Broeckmann C. Densification, deformation, and delamination during co-sintering process of metal–ceramic laminates. J Am Ceram Soc. 2024;e20190. https://doi.org/10.1111/jace.20190

15512916, 0, Downloaded from https://ceramics.onlinelibrary.wiley.com/doi/10.1111/jace.20190 by Rwth Aachen, Wiley Online Library on [28/10/2024]. See the Terms and Conditions (https://onlinelibrary.wiley.com/terms-and-conditions) on Wiley Online Library for rules of use; OA articles are governed by the applicable Creative Commons License

RIGHTSLINK